Supplemental Information: Geometry, mechanics and actuation of intrinsically curved folds

Fan Feng,[1] Klaudia Dradrach,[1] Michał Zmyślony,[1] Morgan Barnes,[1] and John S. Biggins[1]

[1] *Department of Engineering, University of Cambridge, Trumpington St., Cambridge CB2 1PZ, United Kingdom*

(Dated: January 31, 2024)

1. Isometries of intrinsically curved folds

Inspired by the work on curved-fold origami [S1, S2], we compute the exact form of an ICF by assuming that the deformation is isometric and the flanks are developable surfaces. More precisely, given the reference strips (Fig. S1(a)) with geodesic curvatures $\kappa_{g_i}(l)$, the folded configuration Fig. S1(b) is uniquely determined by the arclength parameterized fold (ridge) $\mathbf{r}(l)$.

To compute the shape explicitly, we first establish two important orthonormal frames. The ridge line itself is associated with a unit tangent vector, $\mathbf{t}(l) = \mathbf{r}'(l)$ and orthogonally the curvature vector $\boldsymbol{\kappa} = \mathbf{r}''(l)$, which together define the curve's osculating plane. We may then define the Frenet–Serret frame associated with the ridge-line alone, $\{\mathbf{t}(l), \mathbf{n}(l), \mathbf{b}(l)\}$, where $\mathbf{n}(l) = \boldsymbol{\kappa}(l)/|\boldsymbol{\kappa}|$ is the normalized curvature vector (normal vector) of the ridge and $\mathbf{b}(l) = \mathbf{t}(l) \times \mathbf{n}(l)$ is the bi-normal. Secondly, we have the Darboux frame $\{\mathbf{t}(l), \mathbf{N}(l), \mathbf{B}(l)\}$ associated with the curved ridge $\mathbf{r}(l)$ and one flank surface (for example the red surface in Fig. S1), where $\mathbf{t}(l)$ is again the unit tangent of the ridge, but $\mathbf{N}(l)$ is the unit normal to the flank surface and $\mathbf{B}(l) = \mathbf{t}(l) \times \mathbf{N}(l)$ is a vector in the surface orthogonal to the tangent, and hence pointing away from the ridge. In the Darboux frame, $\mathbf{B}(l)$ and $\mathbf{t}(l)$ thus define the tangent plane of the flank surface.

Since $\mathbf{N}$ is orthogonal to $\mathbf{t}$, we may express it in the Frenet-Serret frame as $\mathbf{N}(l) = \mathbf{b}(l)\cos\alpha + \mathbf{n}(l)\sin\alpha$. The geodesic argument in the main text then gives the fold angles in terms of the curvature:

$$\alpha = (\pm)\arccos(\kappa_{g_i}/|\boldsymbol{\kappa}|). \tag{S1}$$

As the flank is developable, it will be a ruled surface, so its form can be generically expressed as

$$\mathbf{X}(l, v) = \mathbf{r}(l) + v\mathbf{L}(l), \quad v \in [0, V_0], \quad l \in [0, L_0] \tag{S2}$$

where $\mathbf{L}(l)$ is the ruling (or generator) of the surface, $V_0(l)$ is the length of the ruling, and L_0 is the length of the ridge. Furthermore, since the ruling must lie in the surface, we may express it in the Darboux frame as

$$\mathbf{L}(l) = \mathbf{t}(l)\cos\beta(l) + \mathbf{B}(l)\sin\beta(l), \tag{S3}$$

However, not all ruled surfaces are developable. For the flank to be developable, it must satisfy the additional condition $\mathbf{t}(l) \times \mathbf{L}(l) \cdot \mathbf{L}'(l) = 0$, which requires the tangent plane to be invariant along the ruling. After substituting the above form into this condition, a direct algebraic computation [S3] reveals that the flank is only developable if:

$$\beta(l) = \arccos\left[(\tau - \alpha')/\sqrt{(\tau - \alpha')^2 + \kappa^2 \sin^2\alpha}\right], \tag{S4}$$

or equivalently

$$\beta(l) = \operatorname{arccot}\left[(\tau - \alpha')/(\kappa \sin\alpha)\right], \tag{S5}$$

where $\beta(l) \in [0, \pi]$, and $\tau(l) = -\mathbf{n}(l) \cdot \mathbf{b}'(l)$ is the curve torsion. Having thus computed $\beta(l)$, the shape of the flank is then fully specified by (S2), and similarly for the shape of the other flank.

To ensure a solution for a given proposed ridge line, we must have $\cos\alpha \in [-1, 1]$, giving the constraint $|\boldsymbol{\kappa}| \geq |\kappa_{g_i}|$ which restricts the configuration space and the isometry of the folded ICF. Figure S1(c) shows a different isometry that satisfies this constraint. Recalling the sign convention for α_i (also shown in Fig. S1(b)), we have the opening angle given by $\alpha_1 - \alpha_2$, which is larger for a more curved ridge with larger $|\boldsymbol{\kappa}|$.

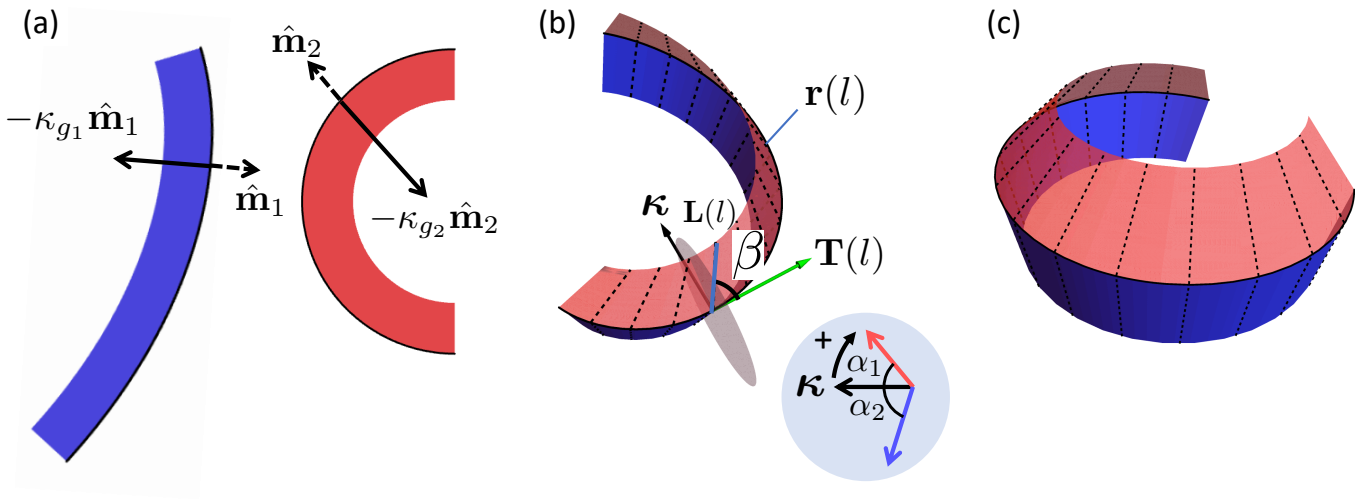

FIG. S1. (a) Reference strips in 2D. (b) Isometry of a folded configuration. (c) A different isometry.

2. Flank bending energy

The bending energy per unit area (bending energy density) of a developable surface is proportional to the mean curvature square H^2 [S4, S5]. Given the explicit form of the developable surface $\mathbf{X}(l, v)$, i.e. Eq. (S2), the mean curvature is given by [S3, S6]

$$H = \frac{\sqrt{|\boldsymbol{\kappa}|^2 - \kappa_g^2}}{2\sin\beta(\sin\beta + v(\kappa_g - \beta'))}. \tag{S6}$$

Notice that the generator $\mathbf{L}(l)$ in Eq. (S2) is a unit vector here for our convenience while the generator direction in [S3, S7] is not normalized, leading to a slightly different presentation. The total bending energy is then given by $E_b = \frac{D}{2}\iint(2H)^2 \mathrm{d}A$, where the area element $\mathrm{d}A$ is computed by $\mathrm{d}A = |\partial_v\mathbf{X} \times \partial_l\mathbf{X}|\mathrm{d}v\mathrm{d}l = (\sin\beta + v(\kappa_g - \beta'))\mathrm{d}v\mathrm{d}l$ and $D = Et^3/[12(1-\nu^2)]$ is the bending stiffness of a plate with Youngs modulus E, thickness t and Poisson ratio ν.

Integrating the bending energy density along the generator yields the dimension-reduced energy, known as the Wunderlich functional [S8], which is given by [S3]

$$\begin{aligned} E_b &= \frac{D}{2}\int_0^{L_0}\left(\int_0^{V_0}(2H)^2(\sin\beta + v(\kappa_g - \beta'))\mathrm{d}v\right)\mathrm{d}l \\ &= \int_0^{L_0}\frac{D}{2}\frac{\kappa^2 - \kappa_g^2}{-(\kappa_g - \beta')\sin^2\beta}\log[1 - (\kappa_g - \beta')w/\sin^2\beta]\mathrm{d}l \end{aligned} \tag{S7}$$

where $\kappa = |\boldsymbol{\kappa}| = |\mathbf{r}''(l)|$ is the scalar curvature of the ridge. In the second expression, we introduce $w = V_0\sin\beta$, which, in the narrow limit is the width of the flank, a more physically relevant quantity than the generator length V_0. For the homogeneous case, we have $\beta = \pi/2$, which reduces this expression to the conical version given in the main text (Main text Eq. 4). In the narrow ribbon limit ($w\kappa_g << 1$), we may take the Taylor expansion of Eq. (S7) and simplify the bending energy as

$$E_{\text{narrow}} = \frac{D}{2}\int_0^{L_0}\frac{\kappa^2 - \kappa_g^2}{\sin^4\beta}w\mathrm{d}l = \frac{D}{2}\int_0^{L_0} w_i\frac{(|\boldsymbol{\kappa}|^2 - \kappa_{g_i}^2 + (\tau - \alpha_i')^2)^2}{|\boldsymbol{\kappa}|^2 - \kappa_{g_i}^2}\mathrm{d}l, \tag{S8}$$

where the second equality follows after substitution for β from Eq. S5, and corresponds to the inhomogeneous narrow result in the main text (Main Text, Eq. 5).

3. Equilibrium configuration

The equilibrium configuration of an ICF is determined by minimizing its total elastic energy, which, using our above results we may write as 1D integral along the ridge. During minimization, the κ_{gi} are fixed, and the angles α_i and β_i

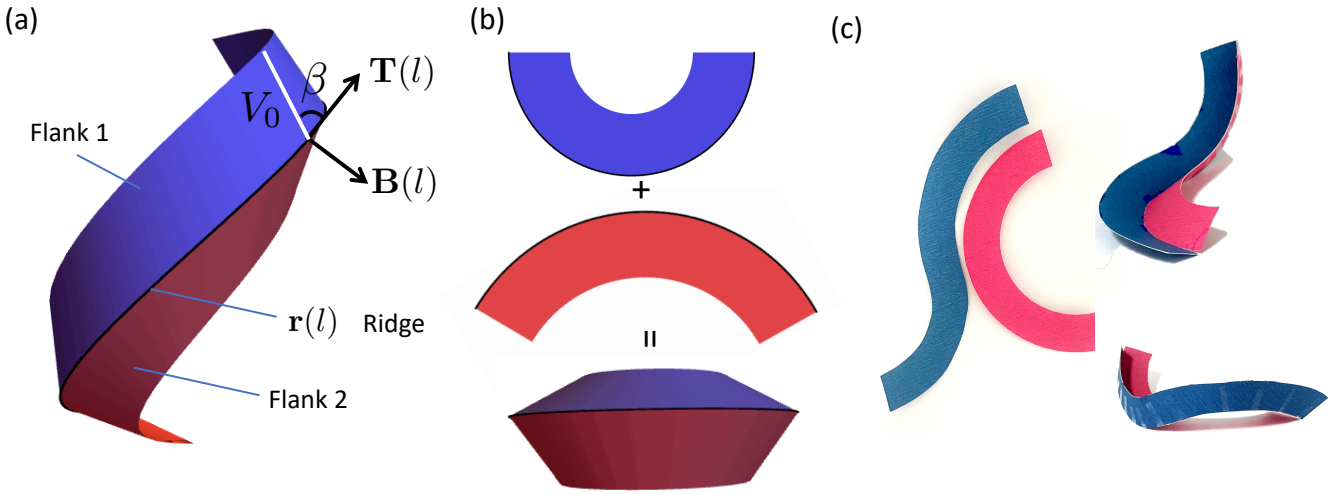

FIG. S2. (a) Geometry of a curved fold. (b) Curved fold with homogeneous geodesic curvatures. (c) Generic curved fold shows non-zero torsion along the ridge.

follow from the form of the ridge line via the kinematic constraints in Eqs. (S5) and (S1). Minimization is thus only over the form of the ridge line, which, according to the fundamental theorem of space curves, is uniquely and exactly specified by the two scalar functions, torsion $\tau(l)$ and curvature $\kappa(l)$. Using our above expressions for the energies as 1D integrals along the ridge line, we thus write the minimization problem as

$$E = \min_{\substack{\tau(l),\ \kappa(l),\ \text{s.t.} \\ \kappa \geq \max(|\kappa_{g_1}|,|\kappa_{g_2}|)}} \int_0^{L_0} \left(\rho_r(\kappa) + \rho_{b_1}(\kappa,\kappa',\tau) + \rho_{b_2}(\kappa,\kappa',\tau)\right) \mathrm{d}l. \tag{S9}$$

In the above expression, ρ_{b_i} is the flank bending energy per unit arclength of the ridge, i.e. the integrand of Eq. (S7), but with β substituted for κ, τ and κ' using Eqs. (S5) and (S1). The ridge energy, ρ_r could take many forms depending on the situation, but generically only depends on κ, as this determines the fold angle. For example, for a freely jointed hinge we have $\rho_r = 0$, a sprung hinge with preferred angle γ has $\rho_r(\kappa) = 1/2(\alpha_1 - \alpha_2 - \gamma)^2 = 1/2(\cos^{-1}(\kappa_{g_1}/\kappa) + \cos^{-1}(\kappa_{g_2}/\kappa) - \gamma)^2$, and a metric mechanics sheet has the form given in the main text, $\rho_r = \frac{1}{4\sqrt{6}}\mu t^{5/2}|\boldsymbol{\kappa}|^{-3/2}(\kappa_{g_1}+\kappa_{g_2})^2$.

The energy in Eq. (S9) can be minimized over τ and κ variationally. Minimization over τ yields a cumbersome algebraic equation, allowing one to express τ as a local algebraic combination of κ and κ'. Substituting this back in, minimization over κ yields a second order Euler-Lagrange equation, $g(\kappa(l), \kappa'(l), \kappa''(l)) = 0$, that must be augmented by two suitable boundary conditions, such as the fold angle at either end of the ICF. Here, we do not attempt a full treatment of this minimization problem, but instead consider some important special cases.

Case 1: homogeneous geodesic curvature ($\kappa_{g_1} = const$, $\kappa_{g_2} = const$). Owing to the translational invarience of the ICF, in this case it is reasonable to search for similarly invarient minimizers, with constant τ and κ, i.e. helices. Minimizing over τ, we now find $\tau = 0$, i.e. the ICF forms a plane curve. Substituting this into β, we find $\beta = \pi/2$, i.e., the generator is perpendicular to the ridge, and thus the length of generator is identical to the width of the strip ($V_0 = w$).

Subsituting this forms for τ and β into the energy, we find the total energy density ρ_E (per unit length of the ridge) as

$$\rho_{\mathrm{E}} = \underbrace{\rho_r(\kappa)}_{\text{ridge energy}} + \underbrace{\frac{1}{6}\mu t^3 w_1 \frac{\kappa^2 - \kappa_{g_1}^2}{-\kappa_{g_1}} \log(1 - \kappa_{g_1} w_1)}_{\text{bending energy of the left flank}} + \underbrace{\frac{1}{6}\mu t^3 w_2 \frac{\kappa^2 - \kappa_{g_2}^2}{-\kappa_{g_2}} \log(1 - \kappa_{g_2} w_2)}_{\text{bending energy of the right flank}}. \tag{S10}$$

Minimization over κ depends on the form of the ridge energy. We consider two special cases:

1. Freely joined folds. The ridge energy of freely joined folds vanishes, i.e., $\rho_r(\kappa) = 0$. Minimizing (S10) over κ under the geometric constraint $\kappa \geq |\kappa_{g_i}|$, we obtain

$$\kappa = \max\{|\kappa_{g_1}|, |\kappa_{g_2}|\}, \tag{S11}$$

meaning that the fold favors a small curvature and hence a small opening angle according to the geometric relation $\alpha_i = \arccos(\kappa_{g_i}/\kappa)$.

2. Metric-mechanic folds. In the metric-mechanic folds using LCE sheets, the effective ridge energy is given by

$$\rho_r = \frac{1}{4\sqrt{6}}\mu t^{5/2}|\boldsymbol{\kappa}|^{-3/2}(\kappa_{g_1}+\kappa_{g_2})^2. \tag{S12}$$

Minimizing the total energy including the ridge energy and the flank bending energy yields the equilibrium κ as

$$\kappa = \frac{3^{\frac{3}{7}}}{2}t^{-\frac{1}{7}}(\kappa_{g_1}+\kappa_{g_2})^{\frac{4}{7}}\left(\frac{\log(1-\kappa_{g_1}w_1)}{\kappa_{g_1}}+\frac{\log(1-\kappa_{g_2}w_2)}{\kappa_{g_2}}\right)^{-\frac{2}{7}}, \tag{S13}$$

or in the narrow ribbon limit,

$$\kappa = (3^3/2^5)^{1/7}\kappa_g^{4/7}t^{-1/7}w^{-2/7}, \tag{S14}$$

as discussed in the main text.

In both cases, these translationally invarient states correspond to global minimizers, but other in-homogeneous morphologies may be obtained by applying non-minimizing boundary conditions on the ICF — in which case, the energy must be minimized variationally.

Case 2: symmetric inhomogeneous geodesic curvature ($\kappa_{g_1}(l) = \kappa_{g_2}(l) \equiv \kappa_g(l) \neq const$). Owing to the difficulty of solving the original Wunderlich functional, we compute the equilibrium state of the symmetric case in the narrow ribbon limit ($w_1 = w_2 = w \ll 1/\kappa_g$). The total elastic energy per unit arclength of the ridge is given by

$$\rho_{\mathrm{E}} = \rho_r(\kappa) + \frac{1}{6}\mu t^3 w\frac{\kappa^2-\kappa_g^2}{\sin^4\beta_1} + \frac{1}{6}\mu t^3 w\frac{\kappa^2-\kappa_g^2}{\sin^4\beta_2}, \tag{S15}$$

where w is the width of the strip. Recalling the sign convention in Sec. 1, we have $\alpha_1 = \arccos(\kappa_{g_i}(l)/|\boldsymbol{\kappa}(l)|) \equiv \alpha$ and $\alpha_2 = -\alpha$. The expressions for the $\sin^4\beta_i$ are then given by

$$\begin{aligned}\sin^4\beta_1 &= \kappa^4\sin^4\alpha/\left[(\tau-\alpha')^2+\kappa^2\sin^2\alpha\right]^2,\\ \sin^4\beta_2 &= \kappa^4\sin^4\alpha/\left[(\tau+\alpha')^2+\kappa^2\sin^2\alpha\right]^2,\end{aligned} \tag{S16}$$

In this case, minimization over τ gives $\tau = 0$ due to the symmetry of the two τ containing terms. Minimization over κ then depends on the form of the ridge energy. Again we consider two special cases:

1. Freely joined folds, $\rho_r(\kappa) = 0$. The global minimizer of ρ_E is $\kappa(l) = \kappa_{g_i}(l)$, as then $\rho_E = 0$, which must be the minimum given ρ_E is strictly positive. This corresponds to the zero energy closed-book state on a plane, with zero ridge energy or bend energy. Other states may be observed by imposing non-minimizing boundary conditions, but the ICF will always be torsion-free.

2. Metric-mechanic folds. In the metric-mechanic folds using LCE sheets, the effective ridge energy is again given by

$$\rho_r = \frac{1}{4\sqrt{6}}\mu t^{5/2}|\boldsymbol{\kappa}|^{-3/2}(\kappa_{g_1}+\kappa_{g_2})^2. \tag{S17}$$

Minimization over κ yields an ODE $g(\kappa(l),\kappa'(l),\kappa''(l)) = 0$ that will determine the shape of the ridge by solving corresponding boundary value problems.

4. Designing ICFs via metric mechanics

A 2D LCE sheet with a patterned director field $\mathbf{n}(x,y)$ will morph into a curved surface in 3D via heating from nematic state to isotropic state. Locally, the sheet contracts by a factor $\lambda_\parallel$ along the director and elongates by a factor $\lambda_\perp$ perpendicular to it, inducing a metric tensor

$$\bar{a}(x,y) = \lambda_\parallel^2\mathbf{n}(x,y)\otimes\mathbf{n}(x,y) + \lambda_\perp^2\otimes\mathbf{n}^\perp(x,y)\mathbf{n}^\perp(x,y). \tag{S18}$$

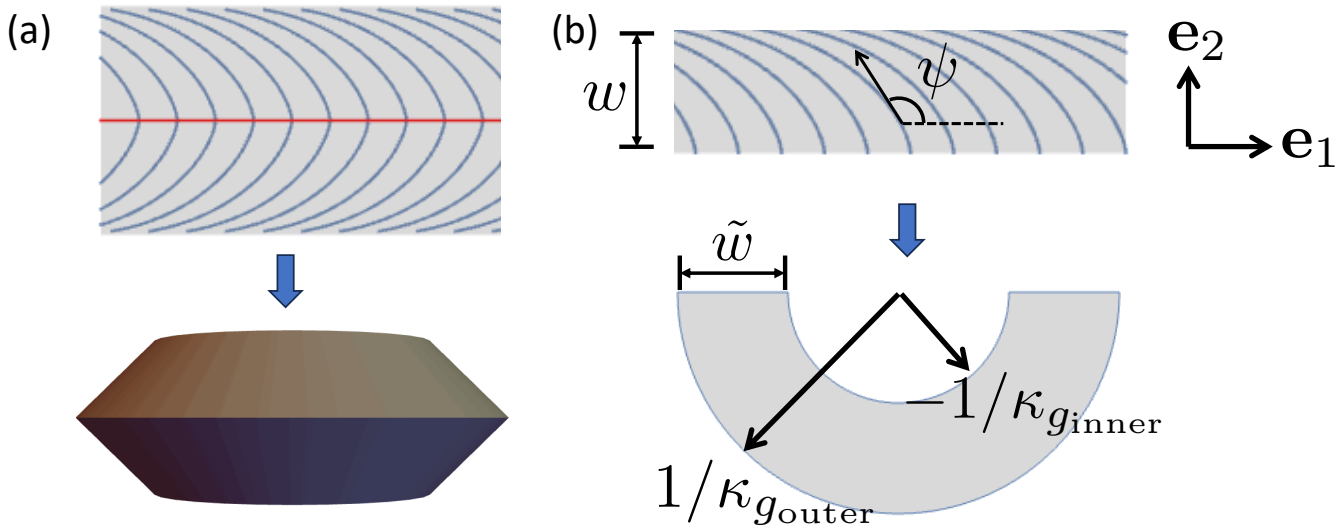

FIG. S3. (a) A translationally invariant pattern morphs into a surface of revolution with a sharp ridge following the exact metric. (b) An individual pattern morphs into an arc strip.

As discussed in the main text, here we seek to design a director pattern with translational symmetry that will morph into a homogeneous ICF, i.e., a surface of revolution with a shape ridge (Fig. S3(a)). Following the main text, we first seek a pattern that will morph a strip into an arc. We thus consider an initially flat strip occupying $0 < y < w$ in with director pattern $\mathbf{n}(x, y) = \cos\psi(x, y)\mathbf{e}_1 + \sin\psi(x, y)\mathbf{e}_2$, as shown in Fig. S3(b). A direct application of the *Theorema Egregium* [S9] shows that the Gaussian curvature of the strip after actuation will be [S10, S11]:

$$K = (\lambda_\parallel^2 - \lambda_\perp^2)\left[\cos(2\psi)\left(\left(\frac{\partial\psi}{\partial y}\right)^2 - \left(\frac{\partial\psi}{\partial x}\right)^2 + \frac{\partial^2\psi}{\partial x\partial y}\right) + \frac{1}{2}\sin(2\psi)\left(\frac{\partial^2\psi}{\partial x^2} - 4\frac{\partial\psi}{\partial x}\frac{\partial\psi}{\partial y} + \frac{\partial^2\psi}{\partial y^2}\right)\right]. \tag{S19}$$

A similar direct computation [S12, S13] shows that a translationally-invariant ($\psi(x, y) = \psi(y)$) straight line in the $\mathbf{e}_1$ (length) direction will, after actuation, have geodesic curvature

$$\kappa_g = \frac{-\left(\frac{\lambda_\perp}{\lambda_\parallel} + \frac{\lambda_\parallel}{\lambda_\perp}\right)\frac{\mathrm{d}\psi}{\mathrm{d}y}\sin\psi\cos\psi}{\sqrt{\lambda_\parallel^2\cos^2\psi + \lambda_\perp^2\sin^2\psi}}, \tag{S20}$$

where $\psi(y)$ is the director angle along the line in the reference state.

We search for a translationally invariant pattern $\psi(x, y) = \psi(y)$ such that the actuated state is an arc-like strip in 2D. We thus set $K = 0$, so that the Gauss equation reduces to $\cos(2\psi)(\partial_y\psi)^2 + (1/2)\sin(2\psi)\partial_y\partial_y\psi = 0$. Solving, we obtain

$$\psi(y) = \frac{1}{2}\arccos(c_1 y + c_2) \tag{S21}$$

where c_1 and c_2 are constants of integration. To achieve the maximal actuation, we choose the constants c_1, c_2 so that the director is parallel and perpendicular to the lower and upper boundaries, leading to the form:

$$\psi(y) = \frac{1}{2}\arccos(2y/w - 1). \tag{S22}$$

Substituting this into Eq. S20, the geodesic curvatures of the boundaries following the sign convention in Fig. S1 and Fig. 2 are

$$\kappa_{g_{\text{inner}}} = \frac{\lambda_\parallel^2 - \lambda_\perp^2}{2w\lambda_\parallel^2\lambda_\perp}, \quad \kappa_{g_{\text{outer}}} = \frac{-\lambda_\parallel^2 + \lambda_\perp^2}{2w\lambda_\parallel\lambda_\perp^2}. \tag{S23}$$

Since these are uniform, the pattern thus does morph the strip into an arc, with inner and outer radii $-1/\kappa_{g_{\text{inner}}}$ and $1/\kappa_{g_{\text{outer}}}$, as shown in Fig. S3. Accordingly, the width of the strip after actuation is $\bar{w} = 1/\kappa_{g_{\text{inner}}} + 1/\kappa_{g_{\text{outer}}}$.

As shown in the main text and Fig. S4, stitching together two strips in different ways will result in four types of ICFs, classified as symmetric positive (S+), symmetric negative (S-), asymmetric positive (A+) and asymmetric negative (A-), based on the concentrated GC and the symmetry. Following the sign convention in the main text, the concentrated GCs, i.e. $\kappa_{g_1} + \kappa_{g_2}$, are $2\kappa_{g_{\text{outer}}}$ (S+), $2\kappa_{g_{\text{inner}}}$ (S-), $\kappa_{g_{\text{outer}}}$ (A+) and $\kappa_{g_{\text{inner}}}$ (A-), respectively. In each case, the stitching trivially obeys the basic rule of metric compatibility, as the director is continuous across the boundary, so the two pattern regions agree on the interface's length. The patterns can also be joined in additional ways, by taking interfaces with a discontinuous director, provided the interfaces bisect the directors on either side [S13].

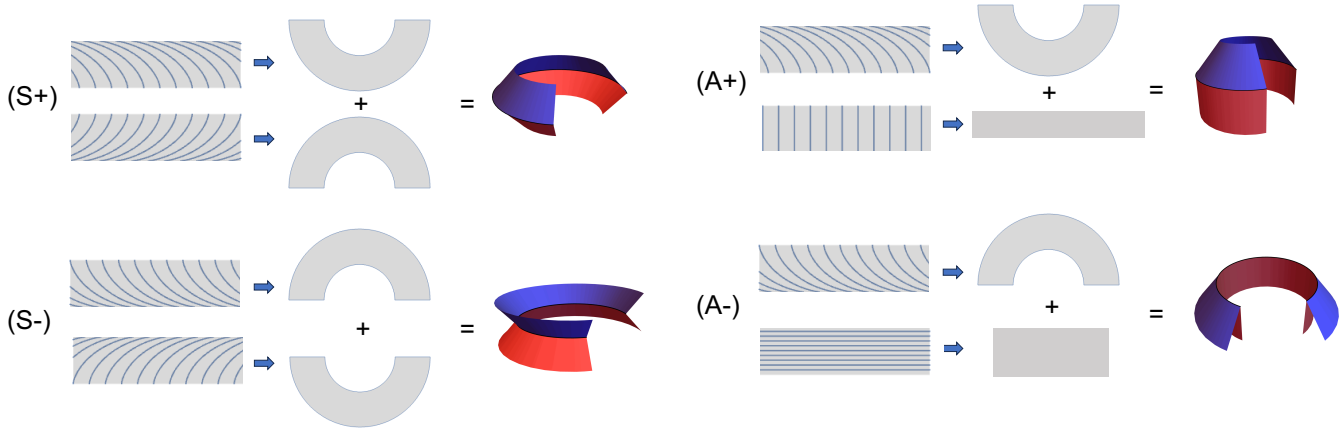

FIG. S4. Constructions of four types of ICFs.

5. Ridge energy for LCE sheets

Following the exact metric, the metric-mechanic ICF will form a sharp ridge after actuation. However, this configuration is not physically observed, as such a sharp ridge would have divergent transverse curvature and hence infinite bending energy. Instead, a relaxed shape with a smooth ridge is observed in experiments and simulations, which emerges via energy minimization involving a stretch-bend trade-off. Here we quantify this ridge energy for LCE sheets. Our result can then be minimized, along with the flank bending energies, to predict the observed form of an unloaded LCE ICF. The code related to this section is released at GitHub `https://github.com/fengfan628/intrisically_curved_folds` with a CC-BY-4.0 license.

5.1. Exact energy for ridge relaxation

We start by considering a homogeneous ICF that follows an exact isometry with curvature κ. Such an ICF will form a surface of revolution consisting of two conical flanks meeting at a sharp ridge with radius $R_0 = 1/\kappa$. We show such an (R, Z) cross-section of such a shape in Fig. S5, alongside the actual surface of revolution, that is generated by rotating the 2D wedge-like cross-section about the axis Z. As ever, the fold angles α_i follow kinematically from the κ and the κ_{gi} that define the fold. In the (R, Z) plane, this reference curve is given by

$$\bar{R}(s) = \begin{cases} R_0 - s\cos\alpha_1, & s \geq 0 \\ R_0 + s\cos\alpha_2, & s < 0 \end{cases}, \quad \bar{Z}(s) = s\sin\alpha_1 \tag{S24}$$

where s is the arclength of the curve. The reference configuration possesses a sharp ridge at $s = 0$ when $\alpha_1 + \alpha_2 \neq \pi$.

To compute the analytical form $(R(s), Z(s))$ of the blunted ridge by energy minimization, we consider the surface as a thin sheet of incompressible Neo-Hookean elastomer with thickness t. The total elastic energy E contains two contributions, the bending energy E_b and the stretching energy E_s, with the forms [S14]

$$E_s = \iint \frac{\mu t}{2}\left(\lambda_1^2 + \lambda_2^2 + \frac{1}{\lambda_1^2\lambda_2^2} - 3\right) \mathrm{d}S \tag{S25}$$

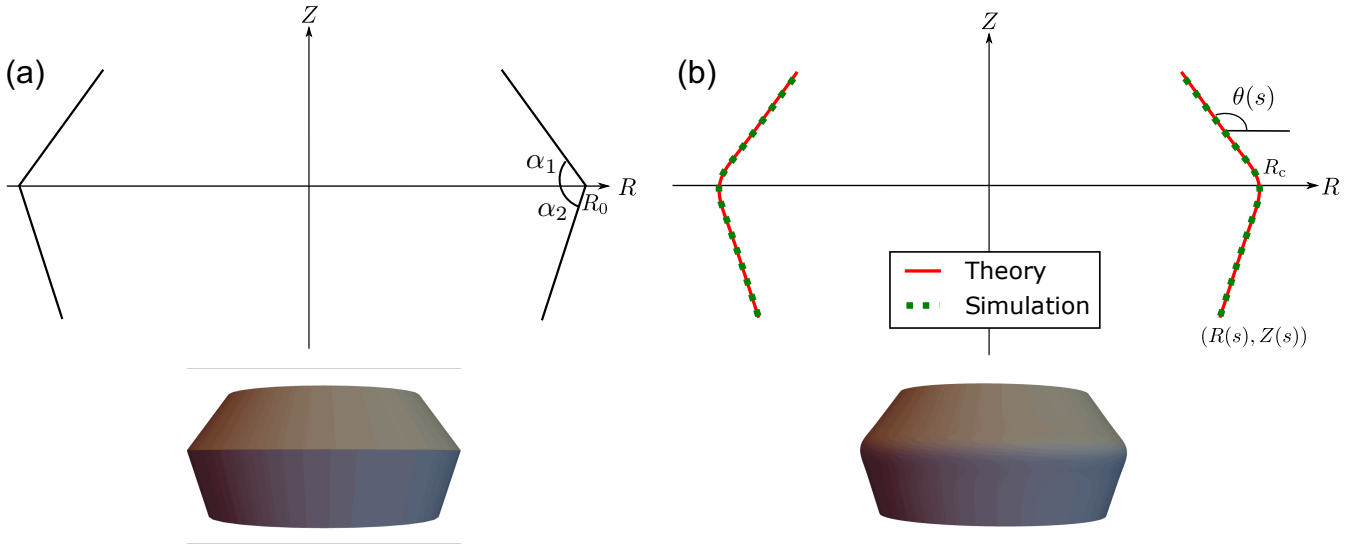

FIG. S5. (a) (R, Z) slice of the initial surface of revolution with a sharp ridge. (b) Blunted ridge $(R(s), Z(s))$ after energy minimization. The parameters are: $R_0 = 1$, $t = 0.01$, $\alpha_1 = 0.3\pi$, $\alpha_2 = 0.4\pi$.

and

$$E_b = \iint \frac{\mu t^3}{6}(\kappa_1^2 + \kappa_2^2 + \kappa_1\kappa_2)\mathrm{d}S \tag{S26}$$

where μ is the shear modulus, λ_i are the (in-plane) principal stretches away from the exact isometry, and κ_i are the principal curvatures of the surface. Normally, the higher thickness scaling of the bending energy makes it negligible compared to stretch, so that the stretch energy effectively becomes a constraint limiting consideration to isometric deformations. In such cases, the bend acts only as a tie break, choosing the bend-energy minimizing isometric deformations. However, here the available isometry has divergent bend, so a non-trivial trade-off between the two must occur.

In the case of a homogeneous ICF, both the reference and relaxed shapes are surfaces of revolution, whose shapes can be described by the slice $(R(s), Z(s))$ in 2D. Accordingly, the principal stretches may be given by

$$\lambda_1 = R(s)/\bar{R}(s), \quad \lambda_2 = \sqrt{R'(s)^2 + Z'(s)^2} \tag{S27}$$

and the principal curvatures given by

$$\kappa_1 = \frac{-R''Z' + R'Z''}{\sqrt{R'^2 + Z'^2}}, \quad \kappa_2 = \frac{Z'/R}{\sqrt{R'^2 + Z'^2}}. \tag{S28}$$

Substituting these forms into E_s and E_b, one obtains an energy that is a simple functional of $R(s)$, $Z(s)$ and their first and second derivatives.

5.2. Full numerical relaxation

The most direct route to finding the shape of the ridge is then to minimize this energy numerically, which we do in Python (also in Mathematica) using a simple 1D finite element scheme. The 1D reference and relaxed curves in the (R, Z) plane are discretized correspondingly. The resulting stretches (S27) and principal curvatures (S28) are computed numerically in a finite element scheme. Then we use the BFGS method in scipy to minimize the total elastic energy $E_s + E_b$ in (S25) and (S26), which leads to the relaxed shape. See GitHub `https://github.com/fengfan628/intrisically_curved_folds` for more detail. An example of such a solution is the "simulation" curve in Figs. S5(b), which, as expected, shows the sharp crease relaxing into a smooth structure.

5.3. Analytic relaxation in thin and nearly cylindrical limit

Our simulations show that blunting is confined to a small region around the ridge, that, as expected, becomes ever smaller in the thin limit, as the ridge comes closer to the sharp true isometry. To obtain further theoretical insight, we use this fact, and our simulations, to make several approximations that then allow a simple analytic solution for the ridge shape. Post-hoc, we see that the approximations are self-consistent in the thin limit, $t \ll R_0$.

Firstly, we assert that the strains are geometrically small (though the rotations may be large), that is, $\lambda_1 = 1 + \epsilon_1$ and $\lambda_2 = 1 + \epsilon_2$ with $\epsilon_1 \ll 1$ and $\epsilon_2 \ll 1$. The stretching energy may then be expanded in terms of ϵ_1 and ϵ_2 as

$$E_s = \frac{\mu t}{2}(4\epsilon_1^2 + 4\epsilon_2^2 + 4\epsilon_1\epsilon_2) + \text{higher order terms.} \tag{S29}$$

Secondly, we assume the elastomer is able to relax to its minimizing strain in the generator direction, leading to $\epsilon_2 = -\epsilon_1/2$. This assumption is equivalent to assuming the azimuthal hoop stress dominates the ss stress, which is well justified by the simulation results, and self-consistently correct in the subsequent analysis. This second approximation reduces the stretching energy to

$$E_\mathrm{s} = \frac{\mu t}{2}(3\epsilon_1^2) = \frac{Et}{2}\epsilon_1^2 = \frac{Y}{2}\epsilon_1^2 = \frac{Y}{2}\left(\frac{\Delta R(s)}{\bar{R}(s)}\right)^2. \tag{S30}$$

where $E = 3\mu$ is the Young's modulus of the LCE, which is the natural modulus for uniaxial stretches, and $Et = Y$ is the stretching modulus of the sheet as used in the main text.

Thirdly, we assume the bending energy is dominated by the generator bend, κ_1 as this is what diverges in the sharp limit. Defining the angle $\theta(s)$ as the angle between the relaxed curve and the radial direction (see Fig. S5B), then, as strains are small, we simply have $\kappa_1 = \theta'(s)$, so the dominant bending energy is:

$$E_\mathrm{b} = \frac{1}{2}D\theta'(s)^2. \tag{S31}$$

Combining these, leads to the total energy

$$E = \int \left(\frac{Y}{2}\left(\frac{\Delta R(s)}{\bar{R}(s)}\right)^2 + \frac{1}{2}D\theta'(s)^2\right) 2\pi\bar{R}(s)\mathrm{d}s. \tag{S32}$$

To make further progress, we fourthly assume R_0 is large compared to the extent of the blunted crease, so that we may neglect the distinction between $\bar{R}(s)$ and R_0 in the region of interest:

$$E = 2\pi R_0 \int \left(\frac{Y}{2}\left(\frac{\Delta R(s)}{R_0}\right)^2 + \frac{1}{2}D\theta'(s)^2\right) \mathrm{d}s. \tag{S33}$$

Finally, we assume that $\alpha_i \approx \pi/2$, i.e. the surface of revolution is nearly a cylinder, which simplifies the curvature to $\kappa_1 = \theta'(s) \approx \Delta R''(s)$. This approximation is the least well justified, as the α_i are determined from the curvature by kinematics, and, in general, only become nearly cylindrical in the highly curved configuration. Nevertheless, making this approximation, we have the simple energy

$$E = 2\pi R_0 \int \left(\frac{Y}{2}\left(\frac{\Delta R(s)}{R_0}\right)^2 + \frac{1}{2}D\Delta R''(s)^2\right) \mathrm{d}s. \tag{S34}$$

Minimizing variationally over $\Delta R(s)$ yields the Euler-Lagrange equation as

$$\Delta R^{(4)}(s) + \frac{Y}{DR_0^2}\Delta R(s) = 0, \tag{S35}$$

which admits four independent solutions $\Delta R(s) \propto \exp((\pm 1 \pm i)s/f)$, revealing $f = (4R_0^2 D/Y)^{1/4} \propto \sqrt{R_0 t}$ as the emergent length-scale of the blunted domain, where $Y = 3\mu t$ and $D = \frac{1}{3}\mu t^3$. Taking the decaying solutions at infinity, we have

$$\Delta R(s) = \begin{cases} c_1 \exp(-s(1-i)/f) + c_2 \exp(-s(1+i)/f) & s > 0 \\ c_3 \exp(s(1-i)/f) + c_4 \exp(s(1+i)/f) & s \leq 0 \end{cases} \tag{S36}$$

Joining them at $s = 0$ under the conditions $\Delta R(0) = d_1$ and $\Delta R'(0) = d_2$ and then minimizing the total energy E over (d_1, d_2), we have

$$\Delta R(s) = -\frac{f}{4} \exp\left(-|s|/f\right) \left(\cos\alpha_1 + \cos\alpha_2\right) \left(\cos(s/f) - \sin(|s|/f)\right). \tag{S37}$$

The actual form of the surface is then reconstructed as $R(s) = \bar{R}(s) + \Delta R(s)$, and $Z(s) = \int \sqrt{1 - R'(s)^2} \mathrm{d}s$. Despite the numerous approximations, we see in Fig. S5 that this solution agrees almost perfectly with the full numerical solution.

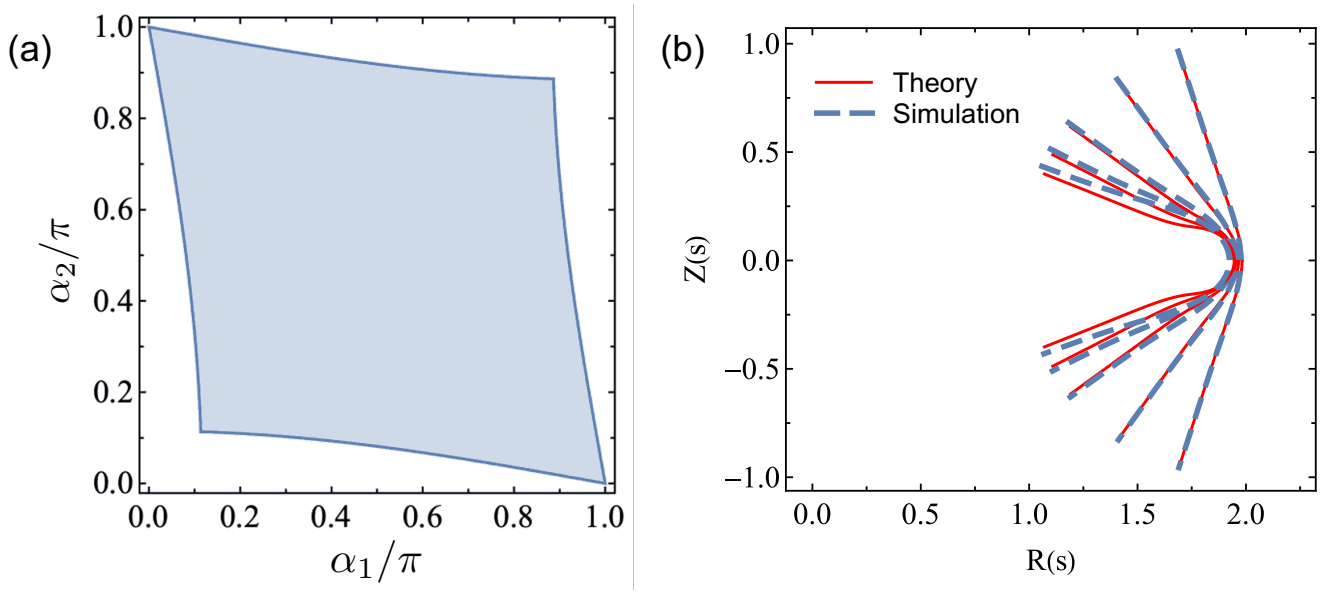

FIG. S6. (a) Admissible domain of (α_1, α_2). (b) Theoretical (Eq. S37) and simulated relaxed shapes for $\alpha_1 = \alpha_2 = (0.12, 0.15, 0.2, 0.3, 0.4)\pi$.

Substituting the relaxed shape (S37), we obtain the effective ridge energy density $\rho_r = E_r/(2\pi R_0)$ as

$$\begin{aligned} \rho_r &= \frac{1}{4\sqrt{6}} \mu t^{5/2} R_0^{-1/2} (\cos\alpha_1 + \cos\alpha_2)^2 \\ &= \frac{1}{4\sqrt{6}} \mu t^{5/2} |\boldsymbol{\kappa}|^{-3/2} (\kappa_{g_1} + \kappa_{g_2})^2. \end{aligned} \tag{S38}$$

Having completed this calculation, we observe that both the length of the blunting region and the associated size of ΔR both scale as $\sqrt{R_0 t}$, which is an intermediate lengthscale, short compared to R_0 but long compared to t. Post-hoc, this intermediate scale justifies all our assumptions, ensuring that our analytic solution is asymptotically exact in the thin limit, $R_0 \gg t$. Precisely, the length of the blunted crease is $\sim \sqrt{R_0 t} \ll R_0$, justifying the approximation $\bar{R}(s) = R_0$ throughout the region of interest. Furthermore, the characteristic size of hoop strain is $\Delta R/R_0 \sim \sqrt{t/R_0} \ll 1$ which vanishes in the thin limit, justifying the small strain approximation. Correspondingly, the azimuthal membrane stress has scale $N\phi\phi = Et(\Delta R/R_0) \sim Et^{3/2}/R^{1/2}$. In contrast, the leading generator stress can be found from vertical force balance as $Nss \sim D\theta''(s) \sim D/f^2 \sim Et^2/R_0$. Hence the ss stress is smaller than the hoop stress by a scaling factor of $\sqrt{t/R_0}$, confirming it is negligible in the thin limit, justifying the approximation $\epsilon_2 = -\nu\epsilon_1$.

Such considerations show that all the key assumptions are justified in the thin limit, except the nearly cylindrical one, $\alpha_i \approx \pi/2$. The equilibrium configuration of a free-floating ICF is given by minimizing total energy consisting of this ridge energy (Eq. S38) and the bending energy of the flanks (Eq. S7). This minimization gives the $\kappa \propto t^{-1/7}$ (Eq. S13), showing that the curvature itself diverges in the thin limit, so, via the kinematic relations, the fold will be almost cylindrical. Thus all the approximations are valid in the thin limit for the equilibrium configuration, explaining the good agreement between theory and numerics/experiment. However, in other circumstances (e.g. under load) one may have a thin ICF that is not nearly cylindrical, so it is useful to probe the range of accuracy/validity of this final approximation. At the extreme limit, the solution is only well defined if $|R'(s)| < 1$, reducing the admissible domain of α_1 and α_2 to that shown in fig. S6. Within this region, we compare the approximate and full numerical

solutions for positive symmetric folds with $\alpha_1 = \alpha_2 \in (0, \pi/2)$ in Fig. S6(b), revealing that a good fit is achieved over a surprisingly wide region of folds, even far from the cylindrical limit, with deviations only becoming significant when $\alpha_1 = \alpha_2 < 0.2\pi$.

5.4. Analytic shape equation for far-from-cylindrical ICFs

The nearly cylindrical approximation is only used to replace $\theta'(s) \to \Delta R''(s)$ in the ICF energy. If this final approximation is invalid, one may instead use the following small-strain relations to substitute ΔR for θ:

$$R(s) = R_c + \int_0^s \cos\theta \mathrm{d}s, \quad Z(s) = \int_0^s \sin\theta \mathrm{d}s. \tag{S39}$$

Making this substitution in the energy Eq. S33, leads to

$$E \approx 2\pi R_0 \int_{-\infty}^{\infty} \left(\frac{Y(R_0 - R_c + \int_0^s (\cos\alpha - \cos\theta(s))\mathrm{d}s)^2}{2R_0^2} + \frac{D(\theta'(s))^2}{2} \right) \mathrm{d}s. \tag{S40}$$

Taking the variation of E with respect to $\theta(s)$ yields the corresponding ODE as

$$\theta^{(4)} = \frac{Y}{DR_0^2}(-\cos\alpha + \cos\theta)\sin\theta + (\theta''^2 + 2\theta'\theta''')\cot\theta - \theta'^2\theta''(1 + \cos^2\theta)\csc^2\theta \tag{S41}$$

where α is the angle between the reference slice and the R axis. For example in Fig. S5(a), $\alpha = \alpha_2$ for $s < 0$ and $\alpha = \pi - \alpha_1$ for $s > 0$. This shape equation can be used to describe the relaxation of thin ICFs, even far from the cylindrical limit. To solve the ODE numerically, we write the generalized vector $\mathbf{u}(s) = (\theta(s), \theta'(s), \theta''(s), \theta'''(s), R(s), Z(s))$ and establish the ODE system $\mathbf{u}'(s) = \mathbf{A}(s)\mathbf{u}(s)$ by substituting (S41), $R'(s) = \cos\theta(s)$, and $Z'(s) = \sin\theta(s)$. Solving the corresponding boundary value problem numerically with solvebvp function in scip of Python gives the relaxed shape of the ridge (see GitHub `https://github.com/fengfan628/intrisically_curved_folds`). We compare the relaxed shapes obtained by the ODE (S41), the analytical solution (S37) and the simulation in Fig. S7. As can be seen, the relaxed shape obtained by the ODE is more accurate when the reference configuration is far from the nearly cylindrical assumption (i.e., α_i is small).

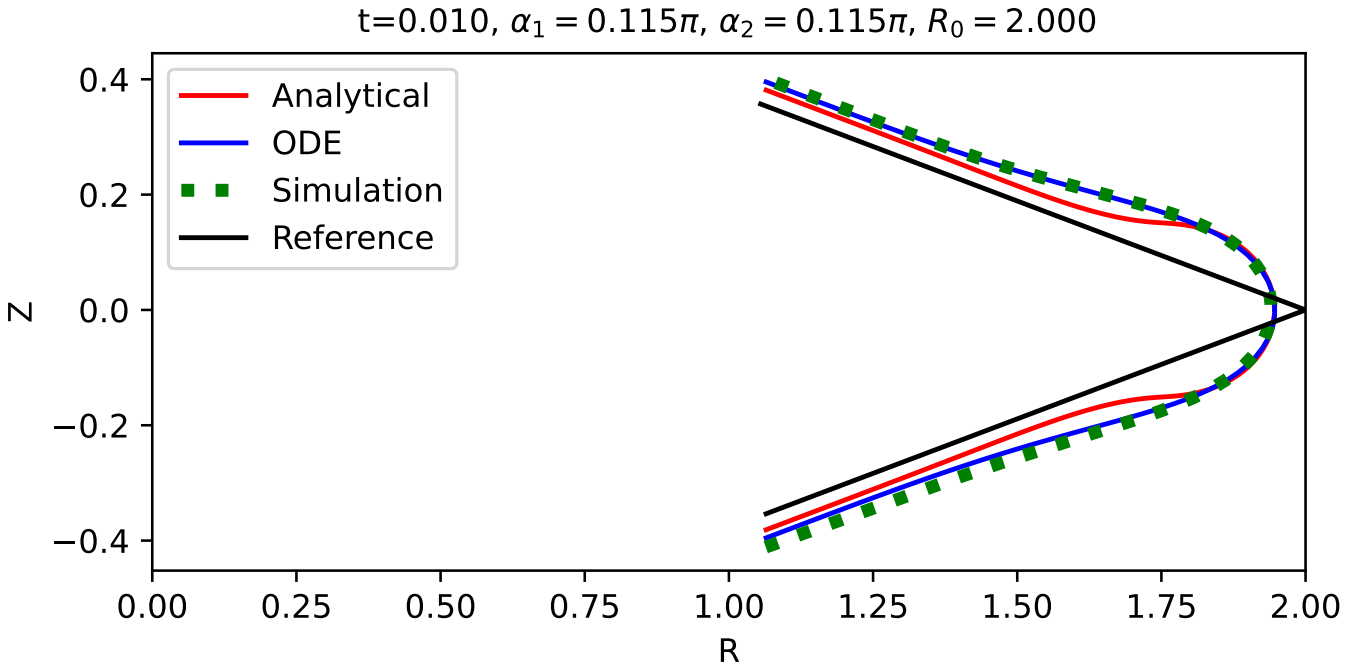

FIG. S7. Relaxed shapes for the ICF with $t = 0.01, \alpha_1 = \alpha_2 = 0.115\pi, R_0 = 2.0$.

6. Experimental: Curved Folds on Paper Models

The curved folds paper models (Figures 4,5 in main text) were constructed using 0.25 mm thick craft paper and scotch tape. The flat individual curves were cut using a Silhouette Studio digital cutter. Asymmetric negative, asymmetric positive, symmetric negative, and symmetric positive curved folds were constructed so that the shared folds had a radius of 4.05 cm and a width 1.3 cm. For the symmetric negative curved fold, two curves (inner radius = 4.05 cm, outer radius = 5.35 cm) were laid flat and the inner curves were taped together with around 18 strips of tape, which acted as hinges, resulting in a flat curve that opened into a 3D curve with the hinge was opened. Similarly, the same protocol was followed for the symmetric positive fold, where curves (outer radius = 4.05 cm, inner radius = 2.75 cm) were taped along the outer edge. Asymmetric negative combined a straight strip of paper (12.72 cm long, 1.3 cm wide) inner edge of a curved (inner radius = 4.05 cm, outer radius = 5.35 cm) paper and the asymmetric positive combined a straight strip of paper (12.72 cm long, 1.3 cm wide) with the outer edge of a curve (outer radius = 4.05 cm, inner radius = 2.75 cm). The curved fold that produced non-zero torsion (Figure 5 in main text) was created by combining a curve with a non-uniform radius of curvature to a curve with a single radius of curvature.

Lifting experiments of the symmetric curved fold paper was model (Figure 4A in main text) as accomplished by attaching tethers to the outer flanges of both sides of the model. When the tethers are pulled the flange opens and the paper model curls into itself and is capable of gripping, lifting, and moving items (a roll of tape is shown).

Strength experiments of the four different curved folds (symmetric negative, symmetric positive, asymmetric negative, asymmetric positive, Figure 4B in main text) were achieved by attaching tethers to both ends of the hinged folds. The paper models were then hung by their top tether and increasingly large weights were attached to the bottom tether and images were taken to determine the weight thresholds where the paper models buckled out of plane.

7. Experimental: The LCE Intrinsically Curved Folds

7.1. 3D printing of LCE

As discussed in the main text (section: Materials and Methods), in order to print all LCE ICFs and the grippers, careful calibration of printing parameters is needed. A more detailed protocol is as follows. First, the printing bed was leveled, and the nozzle of the syringe was placed above the PVA-coated glass such that it was touching the glass, but not pressing it. Second, the syringe with LCE ink (after oligomerization) was installed in the printer, and heated from room temperature to 80°C, and this temperature was maintained for 30 mins. Thirdly, to select optimal printing parameters, a calibration pattern was printed, as shown in Fig. S8. The calibration pattern was composed of a grid of linear samples, differentiated by print speed, line separation, and priming duration (Fig. S8(a)). Following calibration, the printing parameters mentioned in the main text were chosen to obtain repeatable prints with good alignment. We found that print speed, extrusion rate and line separation could be held constant between batches of ink, but priming duration was reoptomised for each batch.

Print patterns were generated using Vector Slicer software for automatic slicing of director patterns. The associated code release is available under `https://github.com/zmmyslony/vector_slicer/releases/tag/publication`.

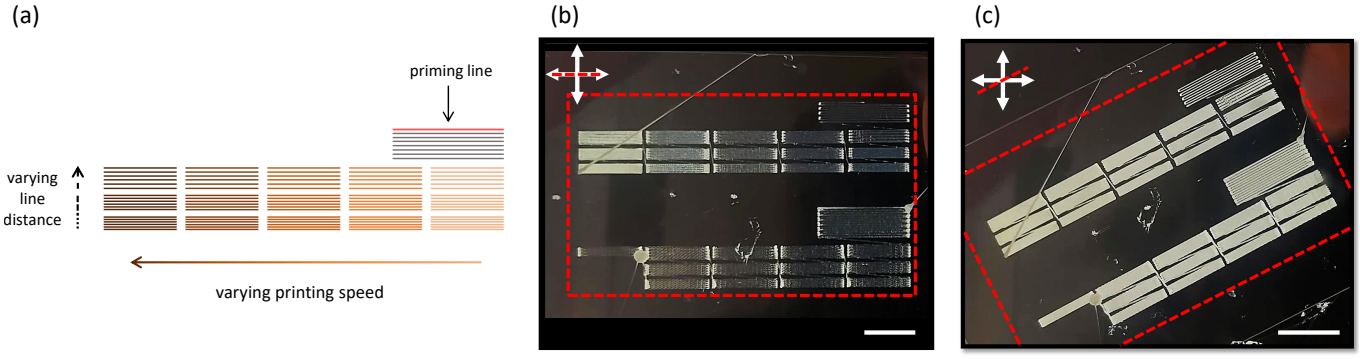

FIG. S8. (a) A scheme of the calibration pattern. (b) and (c) printed calibration patterns seen through crossed polarizers while sample was rotated (white arrows in top left corner; red dotted lines present position of a glass slide against crossed polarizers). Scale bars are 1 cm.

7.2. Characterization of LCE monodomain samples

The thickness of linear samples with different numbers of printed layers was measured with digital calipers before actuation, showing that each layer contributed around 100 μm of thickness (Fig. S9.)

The swelling ratio for printed LCEs submerged in toluene was measured for linear samples with varying thicknesses (3-8 - layers). As seen in Fig. S10, the in-plane swelling ratios are $\lambda_{\parallel} \approx 0.9$ and $\lambda_{\perp} \approx 2.4$, independent of thickness. Interestingly, swelling in the thickness direction itself is slightly less than $\lambda_{\perp}$, which we attribute to the corrugated nature of the print.

The thermal strain of an LCE 3D-printed sample with linear alignment was characterized on a hot plate. Five samples with planar dimensions 2 cm $\times$ 1 cm and four printed layers were placed simultaneously on the hot plate, and elongation parallel and perpendicular to alignment (printing direction) was measured 5 min after the temperature was set. The resulting data are presented in Fig. S11 (with standard error bars), showing that spontaneous stretches were $\lambda_{\parallel} = 0.5$ and $\lambda_{\perp} = 1.33$ by the isotropic state.

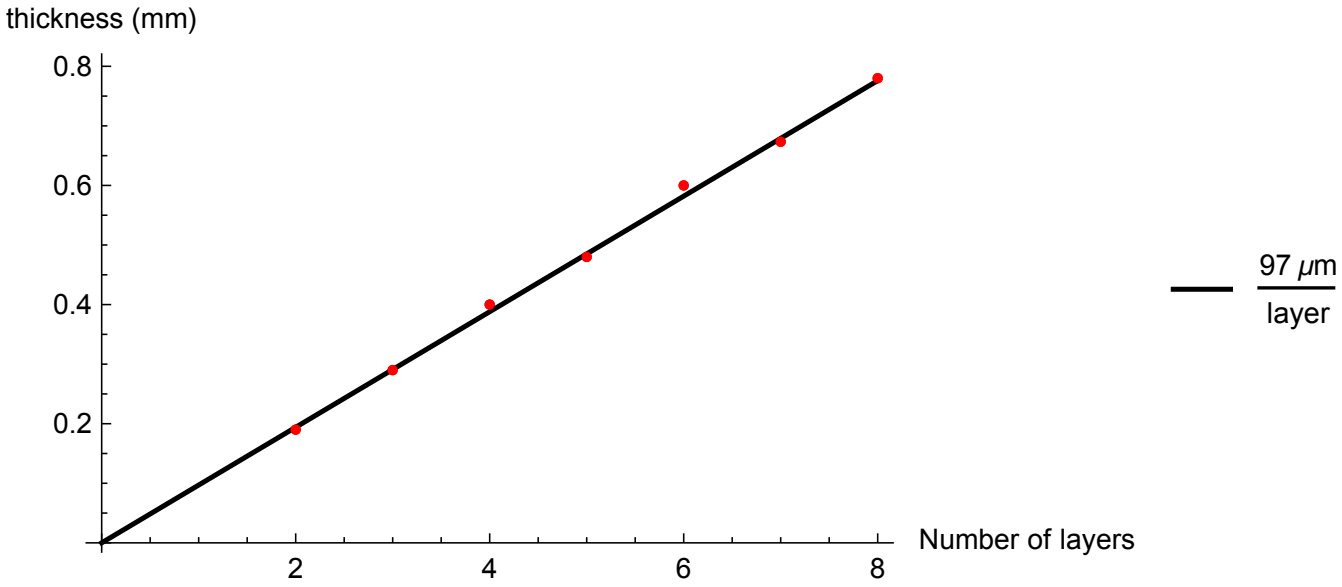

FIG. S9. Thickness (unactuated) of linear patterns with different numbers of printed layers.

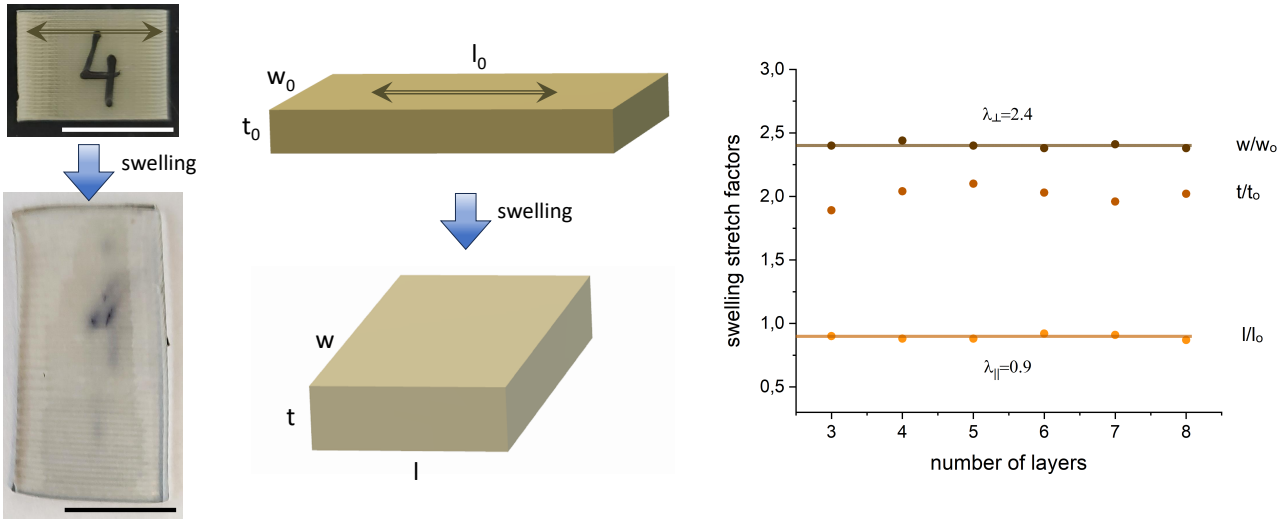

FIG. S10. Swelling strains for for 3D-printed samples with linear alignment. Left: photograph of a four layer sample before and after swelling. Middle: schematic defining the stretch ratios. Right: Swelling ratios for LCE monodomains with varying numbers of printed layers.

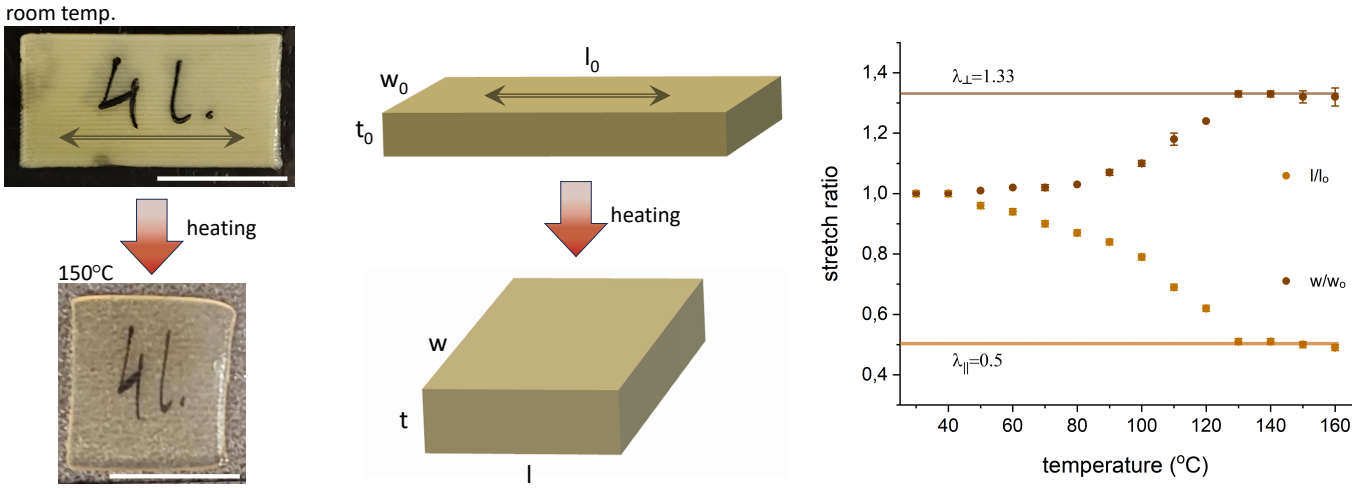

FIG. S11. Thermal strain for 3D-printed samples with linear alignment. Left: photograph of 4-layer sample before and actuation on a hotplate. Middle: schematic defining the stretch ratios. Right: Planar stretch ratios as a function of temperature. Standard errors, with $n = 5$ samples.

8. Movie captions

M1. Kinematics of a curved-fold origami.

M2. Kinematics of a symmetric positive (S+) fold.

M3. Kinematics of a symmetric negative (S-) fold.

M4.Kinematics of an asymmetric positive (A+) fold.

M5. Kinematics of an asymmetric negative (A-) fold.

M6. Gaussian gripper: simulation and experiment.

M7. A Gaussian gripper lifting a load up to 40x the gripper's own weight.

M8. A Gaussian gripper lifting a wide range of objects.

[S1] J. P. Duncan and J. Duncan, Folded developables, Proceedings of the Royal Society of London. A. Mathematical and Physical Sciences **383**, 191 (1982).

[S2] D. Fuchs and S. Tabachnikov, More on paperfolding, The American Mathematical Monthly **106**, 27 (1999).

[S3] T. Yu, I. Andrade-Silva, M. A. Dias, and J. Hanna, Cutting holes in bistable folds, Mechanics Research Communications , 103700 (2021).

[S4] B. Seguin, Y. chao Chen, and E. Fried, Closed unstretchable knotless ribbons and the Wunderlich functional, Journal of Nonlinear Science , 1 (2020).

[S5] R. E. Todres, Translation of W. Wunderlich's "On a developable Möbius band", Journal of Elasticity **119**, 23 (2015).

[S6] R. Wilson, A note on the ruled surface, Edinburgh Mathematical Notes **30**, i (1937).

[S7] E. Starostin and G. Van Der Heijden, The shape of a Möbius strip, Nature materials **6**, 563 (2007).

[S8] W. Wunderlich, Über ein abwickelbares möbiusband, Monatshefte für Mathematik **66**, 276 (1962).

[S9] B. O'neill, *Elementary differential geometry* (Elsevier, 2006).

[S10] H. Aharoni, E. Sharon, and R. Kupferman, Geometry of thin nematic elastomer sheets, Physical Review Letters **113**, 257801 (2014).

[S11] C. Mostajeran, Curvature generation in nematic surfaces, Physical Review E **91**, 062405 (2015).

[S12] D. Duffy and J. S. Biggins, Defective nematogenesis: Gauss curvature in programmable shape-responsive sheets with topological defects, Soft Matter **16**, 10935 (2020).

[S13] F. Feng, D. Duffy, M. Warner, and J. S. Biggins, Interfacial metric mechanics: stitching patterns of shape change in active sheets, Proceedings of the Royal Society A **478**, 20220230 (2022).

[S14] D. Duffy, L. Cmok, J. Biggins, A. Krishna, C. D. Modes, M. Abdelrahman, M. Javed, T. Ware, F. Feng, and M. Warner, Shape programming lines of concentrated Gaussian curvature, Journal of Applied Physics **129** (2021).